Journal of Catalysis 333 (2016) 51–58

Contents lists available at ScienceDirect

Journal of Catalysis

journal homepage: www.elsevier.com/locate/jcat

Priority Communication

Ethylene hydrogenation on supported Ni, Pd and Pt nanoparticles: Catalyst activity, deactivation and the d-band model

Andrew S. Crampton [a], Marian D. Rötzer [a], Florian F. Schweinberger [a], Bokwon Yoon [b], Uzi Landman [b], Ueli Heiz [a,*]

[a] Technische Universität München, Lehrstuhl für Physikalische Chemie, Zentralinstitut für Katalyseforschung und Fakultät für Chemie, Lichtenbergstr. 4, 85748 Garching, Germany
[b] School of Physics, Georgia Institute of Technology, Atlanta, GA 30332-0430, USA

ARTICLE INFO

Article history:
Received 20 July 2015
Revised 29 September 2015
Accepted 13 October 2015

Keywords:
Model catalysis
Nickel
Palladium
Platinum
d-band
Ethylene de-/hydrogenation

ABSTRACT

Ethylene hydrogenation catalyzed at 300 K by 1–1.5 nm nanoparticles of Ni, Pd and Pt supported on MgO (100) with a narrow size-distribution, as well as the deactivation under reaction conditions at 400 K, was investigated with pulsed molecular beam experiments. Ni nanoparticles deactivate readily at 300 K, whereas Pd particles deactivate only after pulsing at 400 K, and Pt particles were found to retain hydrogenation activity even after the 400 K heating step. The hydrogenation turnover frequency normalized to the number of particles exhibited the trend, Pt > Pd > Ni. The activity/deactivation was found to scale with the location of the particles' d-band centroid, ε_c, with respect to the Fermi energy of the respective metals calculated with density-functional theory. An ε_c closer to the Fermi level is indicative of a facile deactivation/low activity and an ε_c farther from the Fermi level is characteristic of higher activity/impeded deactivation. CO adsorption, probed with infrared reflection absorption spectroscopy was used to investigate the clusters before and after the reaction, and the spectral features correlated with the observed catalytic behavior.

1. Introduction

The correlation between the electronic structure and the catalytic activity of materials is one of the fundamental principles underlying the understanding, and systematization of investigations in heterogeneous catalysis. It is also a powerful aid in the selection and design of catalysts, and the interpretation of trends measured across the periodic table. For transition metal catalysts, the d-band model has been particularly useful in investigating and systematizing the above correlation [1–3]. For model heterogeneous catalysis, ethylene hydrogenation represents the most basic hydrogenation reaction catalyzed by noble metals and as such it has been thoroughly investigated on Ni, Pd, and Pt single crystals [4–11], small particles [12–17], as well as a variety of supported metal catalysts [18]. A theoretical study of the ethylene hydrogenation on pseudomorphic Pd films grown on different metal single crystals, employing the d-band model, concluded that the activation barriers for hydrogenation and dehydrogenation depend on the location of the d-band center of the metal catalyst with respect to the Fermi level [19]. Specifically, a d-band center closer to the Fermi level facilitated a lower activation barrier for the dehydrogenation of ethylene to vinyl, and a higher activation barrier for the hydrogenation to ethane.

In this letter we report on an investigation of ethylene hydrogenation on MgO-supported Ni, Pd and Pt nanoparticles with a narrow size distribution of 1–1.5 nm. These investigations were carried out under ultra-high vacuum (UHV) conditions with the use of pulsed molecular beams to study the catalytic behavior of these clusters under isothermal conditions. Infrared reflection absorption spectroscopy (IRRAS), with CO as a probe molecule, was used to probe the catalysts before and after the hydrogenation reaction. Trends in the measured ethylene hydrogenation activity and in the deactivation of the cluster catalysts were found to correlate with the electronic structure of the supported metal particles, in particular the aforementioned d-band centroid model, calculated with first-principles density functional theory (DFT).

2. Methods

All experiments were performed in an UHV chamber with a base pressure of $2 \cdot 10^{-10}$ mbar shown in Fig. 1. The details of the chamber and cluster preparation are described elsewhere [20].

The MgO(100) thin film as support material was grown on a Mo (100) single crystal, and characterized, using techniques that have

* Corresponding author.

http://dx.doi.org/10.1016/j.jcat.2015.10.023
0021-9517/

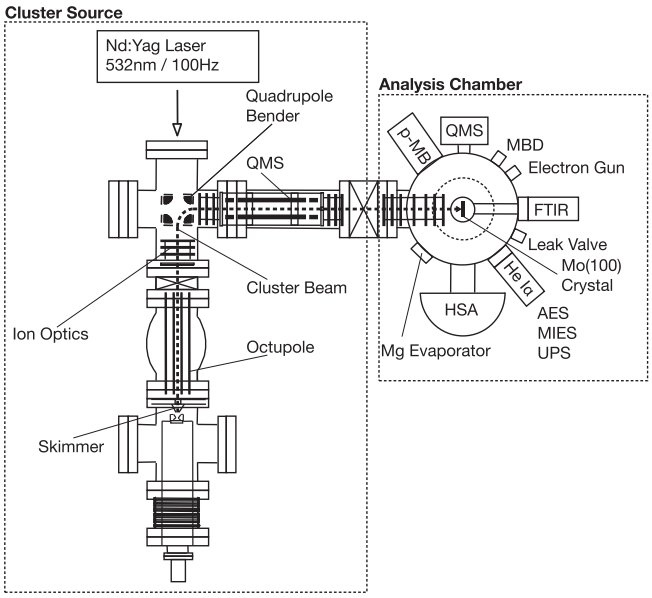

Fig. 1. Schematic of the experimental setup used for this study. On the left, the cluster source is depicted. The 2nd harmonic of a Nd:YAG laser impinges on a rotating metal target and the metal vapor is extracted though the skimmer into the vacuum. It is guided by electrostatic lenses to a bender, and then sent through a QMS which was operated as an ion guide. The particles are then deposited on a MgO (100)/Mo(100) thin film. The right side depicts the analysis chamber with a variety of surface science techniques including pulsed molecular beams, a quadrupole mass analyzer, infrared reflection absorption spectroscopy, Auger electron spectroscopy, Mg evaporator. See [20] for technical details.

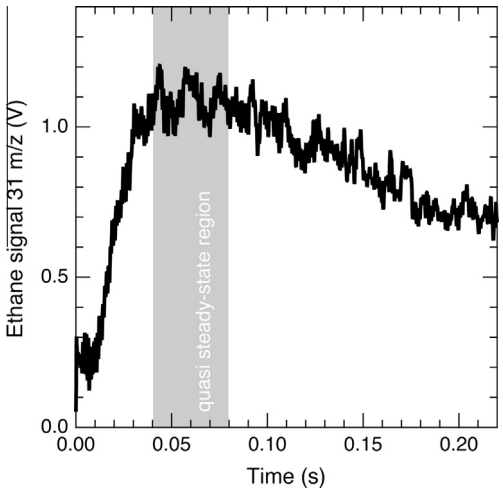

Fig. 2. Representative average of 20 pulses of the ethane ($31m/z$) signal from Pd nanoparticles at 300 K. The area marked in gray defines a region of quasi steady-state conditions, from which the catalytic data were extracted.

been previously described [21]. The Ni (99.98% purity, Goodfellow, England), Pd (99.95%, ESG Edelmetalle, Germany) and Pt (99.95%, Alfa-Aesar, Germany) nanoparticles are generated by a laser vaporization source, coupled with a mass spectrometer. For this work, the quadrupole mass spectrometer (QMS) (Extrel, USA) was operated with only the AC voltage component, which leads to the spectrometer functioning as an ion guide and a high pass mass filter. The size distribution is then determined by the settings of the cluster source [22]. Recent TEM studies on Pt have shown that the particle area distribution of a sample deposited with these settings can be fitted by a log-normal distribution [23–25] and approximately correspond to the size distribution from the source. In these studies a particle size distribution of 1–1.5 nm was determined and this is the expected size range studied in this paper. The coverage is measured by integrating the deposition current and assuming unit charge for all impinging particles. For all measurements, $9 \cdot 10^{12}$ particles were deposited onto the 0.785 cm^2 single crystal.

Catalytic measurements were performed at 300 K using a piezo driven valve, of in house design, to pulse (pulse width = 600 μs, 0.1 Hz) well defined amounts of ethylene (3.5 purity, Westfalen, Germany) onto the sample. The local pressure of ethylene was determined to be $5 \cdot 10^{-7}$ mbar, from the time profile and QMS response from a single ethylene pulse. A background deuterium (100% purity, Westfalen, Germany) pressure of $2 \cdot 10^{-6}$ mbar was applied and the crystal was held approximately 0.5 cm from the piezo valve nozzle and the skimmer leading to the QMS (Balzers QMA 430, Liechtenstein) for reactivity studies.

Fig. 2 shows an average of 20 pulses for the Pd samples. Between a time of 40 ms and 80 ms we define a 'quasi steady state' regime and use this value for the calculation of turnover frequencies (TOF) [26]. The TOF was determined by calibrating the QMS with a monolayer CO TPD from Pt(111) in the same chamber, and determining the sensitivity factor with respect to ethane ($m/z = 30$). The measured mass was $31 = m/z$ as deuterium was used to minimize any possible background signals. Since the QMS calibration was performed with non-deuterated ethane, a systematic error is present in the absolute TOF values calculated. However, it has been shown experimentally that the sensitivity factor of the $m/z = 31$ fragment of $C_2H_4D_2$ with respect to non-deuterated ethane, at an ionizing voltage of 70 V, is approximately a factor of $\frac{1}{2}$ and therefore the values reported here are of the correct order of magnitude [27].

IRRAS (Thermo Electron Corp. Nicolet FT-6700) measurements were performed in single reflection mode, with an external MCT-detector (Thermo Electron Corp., MCTA-TRS), at 100 K after dosing 10 L of CO (256 scans, 4 cm^{-1} resolution). One spectrum was taken with a freshly deposited sample of clusters and the other spectrum after performing the aforementioned catalytic experiment with a freshly deposited sample. This technique of probing metal particles with CO before and after performing ethylene adsorption and/or hydrogenation, has often been used to investigate particle morphology and the presence of carbon deposits [28–32].

For modeling the experimentally obtained size-distribution a representative cluster of 30 atoms for each metal was chosen. To model M_{30}/MgO (M = Ni, Pd, and Pt) systems, we employed a four-layer MgO(100) slab with a calculational cell consisting of 7×6 unit cells; each layer consisted of 42 Mg and 42 oxygen atoms with the atoms in the bottom layer held stationary (at the experimental lattice constant of 4.21 Å) and the atoms in the other three layers allowed to relax to the optimal atomic arrangement; optimal configurations (using a conjugate gradient search) were determined when the calculated energy converged within 0.001 eV. The bare M_{30} cluster was positioned on the MgO(100) surface, and its configuration was optimized, see [33] for details regarding the particle geometry. The calculational supercell, which included the MgO(100) slab and a 24 Å thick vacuum region, was periodically replicated.

The first-principles electronic structure calculations used the density-functional theory (DFT) method employing the VASP-DFT package, using a plane-wave basis with a kinetic energy cutoff of 400 eV, PAW pseudopotentials [34] and the PBE generalized gradient approximation (GGA) for the exchange–correlation potential [35]. Γ-point sampling of the Brillouin zone was used. The angular-momentum projected local density of states (PLDOS) was calculated by using the spherical harmonics, Y_{lm}, projectors (in particular l = 2 for the d-band PLDOS). The PLDOS of the entire cluster

is the sum of the projected contributions calculated for each of the atoms of the adsorbed metal cluster, with the position of the atom taken as the center for the angular-momentum projection and the integration carried out over a sphere of radius 1.22 Å (Ni), 1.37 Å (Pd, Pt) about each of the atoms; this radius is taken as half of the average bond-length to minimize overlap.

3. Results

Fig. 3a displays the pulse-to-pulse ethane signal from deposited Ni, Pd and Pt clusters at 300 K. The pulse-to-pulse signal from the same samples measured at 100 K is also included as a background and can be seen to be approximately zero. The plotted Pd and Pt results also show, in addition, the ethane signal measured at 300 K after exposing the samples to 15 ethylene pulses at 400 K. Since the Ni data show a fast deactivation of the particles after only 15 pulses at 300 K, the effect of heating to 400 K was not probed. For Pd nanoparticles the product (ethane) signal at 300 K slowly decreases as the number of pulses increases, but catalytic activity maintains even after 20 pulses. However, after pulsing the nanoparticles with ethylene at 400 K the sample is observed to have lost all hydrogenation activity. The Pt nanoparticles exhibit a similar behavior at 300 K to that of Pd, but hydrogenation activity persists even after ethylene pulsing at 400 K.

The IR spectra of CO adsorbed on the Ni, Pd and Pt nanoparticles before and after the experiments in Fig. 3a are displayed in Fig. 3b. The Ni spectrum before the reaction shows a single peak at 2088 cm^{-1}, with a broad feature at 1900–1950 cm^{-1} corresponding to linear and bridge bonded CO, respectively. After the reaction has been run, the bridge bonded peak disappears and the linear

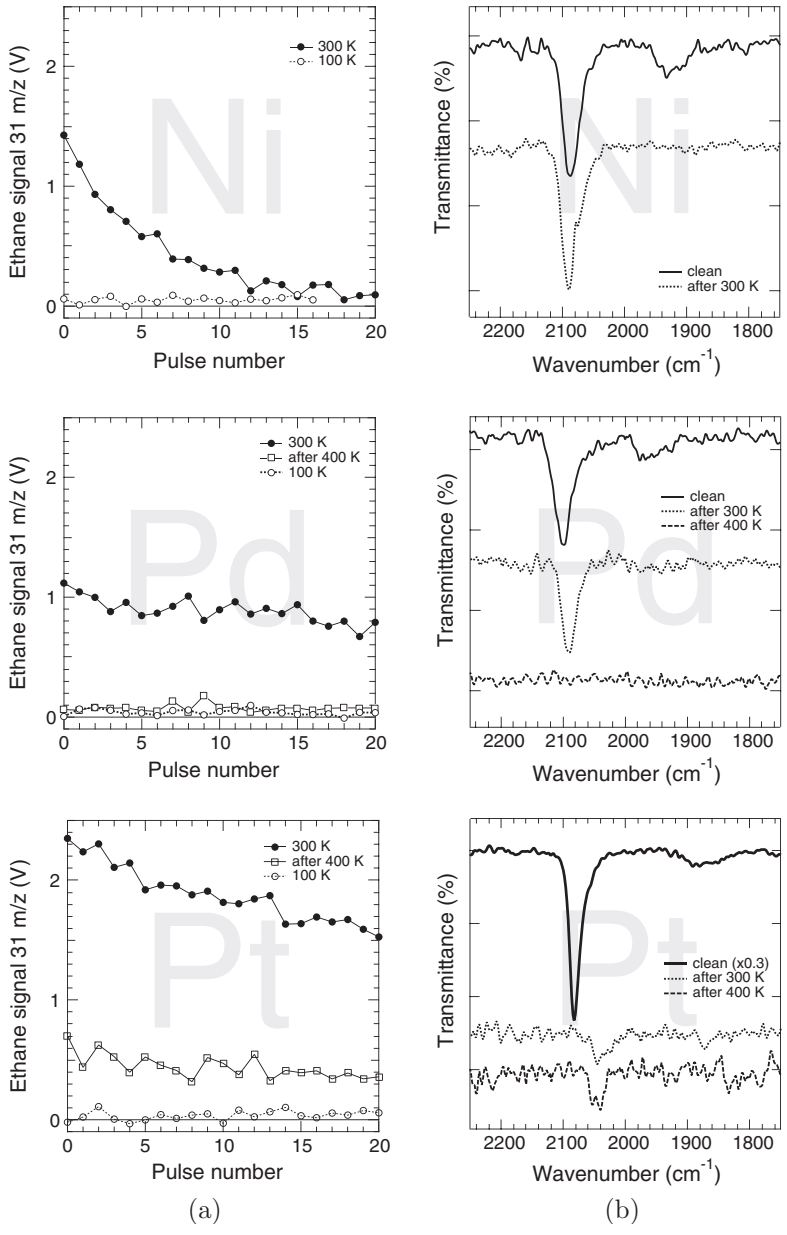

Fig. 3. Pulsed molecular beam (a) and IRRAS (b) data from Ni, Pd and Pt nanoparticles of the size range 1–1.5 nm. In all cases the data in (a) show the ethane signal progression of single ethylene pulses, and the data shown in (b) were recorded before and after the completion of the experiments shown in (a). The Ni data (top panels) in (a) show the pulse-to-pulse ethane signal taken at 300 K and at 100 K, and in (b) measurement of the linear- and bridge-bonded CO stretch on clean Ni nanoparticles and after pulsing at 300 K. The Pd data (middle panels) in (a) depict the pulse-to-pulse data at 100 K, at 300 K, and at 300 K but subsequent to pulsing ethylene at 400 K. The Pd IR spectra in (b) show the linear- and bridge-bonded CO stretch on a clean sample, and after the corresponding experiments displayed in (a), except the one at 100 K. The Pt measurements (bottom panels) in (a) and (b) were performed under the same conditions described for the Pd data.

bonded peak shifts slightly to higher wavenumbers and now has a shoulder at 2075 cm^{-1}. The Pd IR spectrum before the reaction shows the linear and bridge bonded CO species at 2098 cm^{-1} and 1960 cm^{-1}, respectively, as with Ni. Following ethylene pulsing at 300 K the bridge bonded disappears and the linear peak is slightly redshifted to 2088 cm^{-1}. After running the reaction subsequent to ethylene pulsing at 400 K, no CO peak is observed.

The Pt IR spectrum before the reaction shows a linear bonded species on the clean particles at 2082 cm^{-1} and bridge bonded centered at 1870 cm^{-1}. After pulsing at 300 K there is a redshift in the CO stretch and after ethylene pulsing at 400 K, a double peak at 2054 and 2040 cm^{-1} is measured. Both Pt spectra after the two reaction cycles ('300 K' and 'after 400 K', Fig. 3a) display a very strong decrease in signal intensity compared to the Ni (top) and Pd (middle) cases.

A cluster consisting of 30 atoms was chosen as a model for the studied nanoparticle systems, as this size has dimensions similar to the size distribution investigated. To determine optimal structures of the adsorbed 30-atom clusters on the Mg(100) surface we have focused on the Pd_{30} cluster; once alternative structural motifs have been constructed and tested, the optimal ones have been relaxed subject to the characteristic pseudopotentials of the three metals (Ni, Pd, and Pt). On the clean surface of MgO(100) (prior to adsorption of the Pd_{30} cluster), the oxygen atoms of the topmost layer are located 0.053 Å higher (i.e., toward the vacuum) than the Mg atoms. After adsorption of the pyramidal Pd_{30} cluster on the surface, the 16 O atoms in the area covered by the base of the cluster (see Fig. 4) are found to be located 0.009 Å higher than the corresponding 16 Mg atoms. The ground-state structure of the supported Pd_{30} cluster is found to be a square pyramid (Fig. 4a and b), with the energy of the optimal Pd_{30}(pyramid)/MgO system found to be lower by 1.84 eV compared to an alternative (fully relaxed) two-layer structure (Fig. 4c and d). On the other hand, the (vertical) adsorption energy of the two layer Pd_{30} cluster isomer to the MgO(100) surface is slightly higher (E_{ads}(2-layer) = 10.45 eV) than that of the pyramidal cluster (E_{ads}(pyramid) = 10.08 eV); E_{ads} [vertical binding energy, vBE, in Table 1] is calculated as the difference between the total energies of the individual components (free cluster and clean surface, both in the configurations of the optimally adsorbed system) and that of the combined adsorption system Pd_{30}/MgO. As found in earlier first principles investigations, free [36] and supported [37] Pd clusters exhibit spontaneous magnetization. The optimal minimum energy configuration of the Pd_{30} (pyramidal) cluster has a spin state with $N\uparrow - N\downarrow = 4$ (where $N\uparrow$ is the number of spin-up electrons and $N\downarrow$ is the number of spin-down electrons); the energy of this magnetic state is lower by 0.05 eV than that with no magnetic moment, i.e., $N\uparrow = N\downarrow$. In the current investigation we give results for the non-magnetic states of the clusters, because of the very small influence that they have on the geometrical and electronic properties of the adsorbed clusters. Details of the structural parameters for the ground-state pyramidal and 2-layer structural isomers of the 30-atom Ni, Pd and Pt clusters are given in Tables 2 and 3.

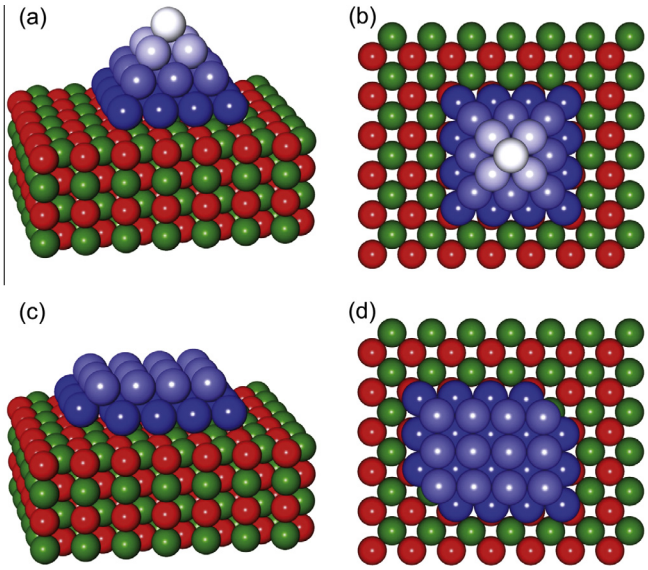

Fig. 4. Optimal structures of pyramidal (a, b) and two-layer (c, d) Pd_{30} clusters adsorbed on a MgO(100) surface. The atoms of the Pd_{30} clusters are colored by a blue color gradient for clarity. The color depends on the distance of the Pd atoms from the MgO surface, with those closer to the MgO surface depicted in a deeper blue color. The Mg atoms are green spheres and the oxygen atoms are red. The adsorbed pyramidal Pd_{30} cluster is 1.84 eV lower in energy than the two-layer cluster. (a) and (b): Pyramidal Pd_{30}. The numbers of Pd atoms from the bottom Pd layer to the top layer are 16, 9, 4, and 1. The spacing between the bottom Pd layer and the topmost O (Mg) atoms under the Pd_{30} cluster is 2.267 Å (2.258 Å). The spacing between the bottom (first) layer and the Pd cluster and the layer above it (second layer) is d_{12} = 1.987 Å. The spacing between the consecutive layers is d_{23} = 1.795 Å and d_{34} = 1.790 Å. The average Pd–Pd bond length on the bottom edge of the Pd_{30} pyramid is 2.66 Å. (c) and (d): Two-layer Pd_{30}. The numbers of Pd atoms of lower and upper Pd layers are 18 and 12. The spacing between the lower Pd layer and the topmost O (Mg) atoms under Pd_{30} is 2.284 Å (2.283 Å). The spacing between two Pd layers is d_{12} = 1.999 Å.

Table 1
Total energy differences and vertical binding energy of the X_{30} cluster to the Mg(100) surface. $\Delta E = E_{tot}[X_{30}(2\text{-layer})/MgO] - E_{tot}[X_{30}(pyramid)/MgO]$ and $vBE = E[\text{frozen } X_{30}] + E[\text{frozen MgO}] - E_{tot}[X_{30}(2\text{-layer})/MgO]$ where X = Ni, Pd, and Pt. E[frozen X_{30}] and E[frozen MgO] denote the total energies of the isolated 30 atom cluster and the bare underlying MgO surface in the geometries they have when the cluster is adsorbed on the surface (for which the total energy is given as $E_{tot}[X_{30}$(pyramid or 2-layer)/MgO]). Energies in units of eV.

	Ni_{30}/MgO	Pd_{30}/MgO	Pt_{30}/MgO
ΔE (eV)	2.47	1.84	3.93
$vBE_{pyramid}$ (eV)	11.09	10.08	10.99
$vBE_{2\text{-layer}}$ (eV)	12.19	10.45	11.87

Table 2
Interlayer and interatomic distances for the pyramidal adsorbed clusters. d_{1-O} is the spacing between the bottom layer of the cluster and the top 16 O (oxygen) atoms under the cluster, d_{1-Mg} is the spacing between the bottom layer of the cluster and the top 9 Mg atoms under the cluster, d_{1-2} is the spacing between the bottom and the 2nd cluster layer, d_{2-3} is the spacing between the 2nd cluster layer and the 3rd cluster layer, d_{3-4} is the spacing between the 3rd cluster layer and the 4th cluster layer. ⟨bl⟩ is the average bond length of the bottom edge atoms of the cluster.

	Ni_{30}(pyramid)/MgO	Pd_{30}(pyramid)/MgO	Pt_{30}(pyramid)/MgO
d_{1-O} (Å)	2.035	2.267	2.272
d_{1-Mg} (Å)	2.107	2.258	2.262
d_{1-2} (Å)	1.557	1.987	1.970
d_{2-3} (Å)	1.622	1.795	1.762
d_{3-4} (Å)	1.659	1.790	1.838
⟨bl⟩ (Å)	2.482	2.664	2.645

Table 3
Interlayer and interatomic distances for the two-layer adsorbed clusters d_{1-O} is the spacing between the bottom layer of the cluster and the top 18 O atoms under the cluster, d_{1-Mg} is the spacing between the bottom layer of the cluster and the top 10 Mg atoms under the cluster, d_{1-2} is the spacing between the bottom and the 2nd cluster layer, and ⟨bl⟩ is the average bond length of the bottom edge atoms of the cluster.

	Ni_{30}(2-layer)/MgO	Pd_{30}(2-layer)/MgO	Pt_{30}(2-layer)/MgO
d_{1-O} (Å)	2.055	2.284	2.271
d_{1-Mg} (Å)	2.123	2.283	2.268
d_{1-2} (Å)	1.583	1.999	1.981
⟨bl⟩ (Å)	2.541	2.691	2.668

4. Discussion

From comparison of the catalytic reactivities of the three metal nanoparticles (Fig. 3a) a clear trend can be established as a function of an elements period within the same group of the periodic table. In particular, the tendency for a group 10 metal to deactivate in the course of ethylene hydrogenation increases as the period decreases – namely, Ni (period 4) exhibits the highest deactivation tendency (see sharp falloff of the activity with increasing number of pulses in Fig. 3a), whereas Pt (period 6) displays a much reduced deactivation (maintains reactivity after ethylene pulsing at 400 K), and Pd (period 5) shows an intermediate behavior (deactivation only after ethylene pulsing at 400 K).

In the case of extended surfaces it has been found (based on the d-electron model [1,2]) that the activation barrier for ethylene hydrogenation increases as the d-band center shifts closer to the Fermi level, while the activation barrier for dehydrogenation, resulting in formation of carbonaceous species (that poison the hydrogenation reaction) decreases [19]. To assess the validity of these results for the case of the nanoparticles investigated here, we show in Fig. 5 the DFT calculated DOS for M_{30}/MgO(100), [M = Ni, Pd and Pt], evaluated for the structure of the representative 30-atom adsorbed cluster shown as inset in the middle panel of Fig. 5, which has been found previously to be the lowest – energy optimal configuration for Pd_{30}/MgO [33]. The cluster d-band centers, $\varepsilon_c^M = E_c^M - E_F$, for M = Ni, Pd, and Pt, where E_F is the Fermi energy of the cluster, obtained from the d-level projected DOS (PLDOS, see red-filled areas in Fig. 5), were calculated to be $\varepsilon_c^{Ni} = -1.33$ eV, $\varepsilon_c^{Pd} = -1.86$ eV, $\varepsilon_c^{Pt} = -2.40$ eV. These values are rather similar to those calculated for the d-band centers in extended (bulk) Ni, Pd, and Pt surfaces −1.29 eV, −1.89 eV and −2.25 eV, respectively [38], and thus the general conclusions drawn about the hydrogenation reaction catalyzed by the extended (bulk) surfaces of these metals [19] are expected to extend to the supported nanoparticles in the size-range of 1–1.5 nm. This expectation is apparent from Fig. 3a for deactivation and quantified in Fig. 6 where the scaling of ε_c^M with the hydrogenation activities of the three nanoparticle systems is depicted. Here, the hydrogenation activity is expressed in terms of the hydrogenation (ethane production) TOF, which has been calculated per particle from the average of pulses showing a constant activity. Fig. 6 illustrates that for the clusters of M = Ni, Pd and Pt studied here the predicted scaling of the hydrogenation reaction TOF with ε_c^M is maintained.

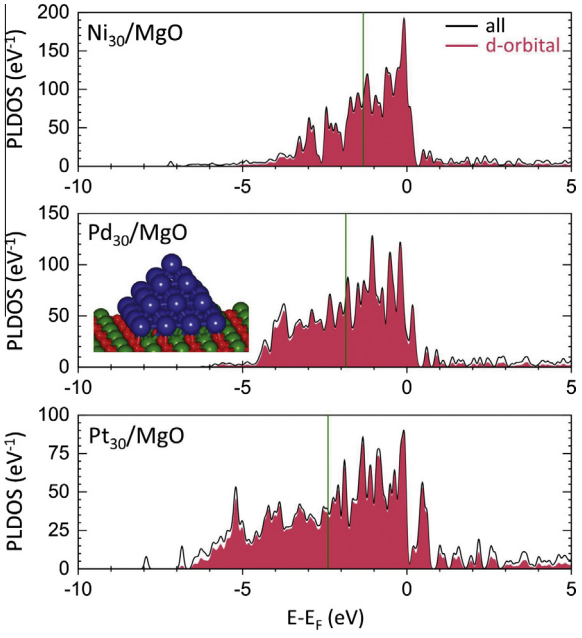

Fig. 5. Density of states (DOS, black line) and d-band projected DOS (PLDOS, red filled) for the optimized pyramidal structures of Ni_{30} (top), Pd_{30} (middle) and Pt_{30} (bottom) clusters adsorbed on Mg(100). The structure of the Pd_{30}/Mg(100) system is shown as an inset in the middle panel (Pd atoms in blue, Mg in green and oxygen in red); the numbers of Pd atoms from the bottom Pd layer to the top layer are 16, 9, 4, and 1 (for geometrical details see Table 2). The calculated d-electron centers, ε_c^M, are marked by green vertical lines.

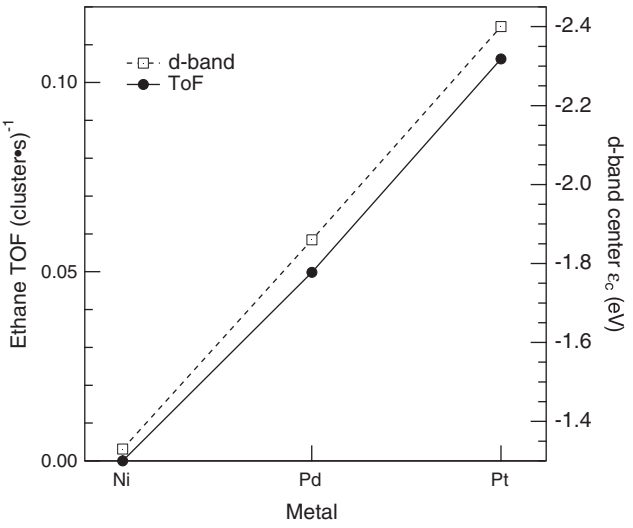

Fig. 6. Ethane TOF for Ni, Pd and Pt nanoparticles plotted against the calculated d-band center, ε_c (see Fig. 5). The closer the d-band center is to the Fermi level, the lower the activity and the more facile the deactivation (see Fig. 3a). The TOF has been calculated from pulse 17 to 20 for all three metals.

While the general behavior of the catalysts can be well rationalized with the d-band model, the microscopic picture is still uncertain. In particular, Ref. [19] only investigated an initial dehydrogenation step to a vinyl intermediate, which may or may not be the final product/intermediate at a given temperature on a given metal.

In order to investigate features of the nanoparticle surface subsequent to reaction, IRRAS of CO (see Fig. 3b) provides a powerful tool, where a decrease in the CO absorption intensity can indicate a loss of adsorption sites and a redshift indicates co-adsorbed carbonaceous species [28–32].

After pulsing at 300 K the signal corresponding to bridge-bonded CO on Pd disappears, but the linearly-adsorbed CO adsorption peak is still visible and 10 cm^{-1} redshifted, see Fig. 3b. The loss of CO adsorption sites from ethylene decomposition on Pd has been previously reported [28,29] and our results support this finding. Following pulsing at 400 K, however, resulting in completely deactivating the catalyst (Fig. 3a), there is no detectable CO adsorption, implying blocking of all CO adsorption sites on the particles by carbon species. Such a complete loss of all CO adsorption sites (down to the detection limit) has, to our knowledge, not been observed previously; Refs. [28,29] only investigated the effect of ethylene decomposition at 300 K, with ethylidyne identified as the resulting surface species [29]. The effect of higher temperatures on further dehydrogenation and subsequent CO adsorption has not been studied, but a temperature-dependent model of ethylene adsorption on Pd nanoparticles has been proposed based on temperature programmed desorption, IRRAS and X-ray photoelectron spectroscopy studies [13]. The authors identified three distinct temperature regions: (i) $T < 300$ K, here ethylene can be π- or di-σ-bonded to Pd particles, with the di-σ species being able

to convert to ethylidyne between 250 and 300 K. (ii) 300 K < T < 400 K, ethylidyne can dehydrogenate further to form C–H surface species. (iii) T > 400 K, in this region a complete dehydrogenation occurs and the particles are covered with carbon deposits. This proposed model explains the results of the CO IRRAS experiments here. At temperatures up to 300 K a limited amount of dehydrogenation occurs, possibly to form ethylidyne, which is evidenced by the loss of bridge bonded CO and slight redshift. At temperatures up to 400 K further dehydrogenation reactions occur, resulting in the blocking of CO adsorption sites (no CO IR peak), and poisoning of the ethylene hydrogenation reaction.

The similarity between the IR spectra taken after the two reaction cycles on Pt indicates that the temperature increase to 400 K has not caused any reduction in CO adsorption capability, but from Fig. 3a has caused a decrease in activity. The activity decrease is likely an effect of accelerated ethylene dehydrogenation at elevated temperatures leading to increased site blocking, as particles in this size range have been previously proposed to suppress ethylene dehydrogenation at 298 K [17]. The presence of a small CO peak after the 400 K step is not unexpected, as CO is able to penetrate an ethylidyne surface layer [31] and dehydrogenated fragments tend to have low saturation coverages due to repulsive interactions [39]. The identification of ethylidyne as the dehydrogenation product on Pt nanoparticles is, however, tenuous at particle sizes smaller than 2 nm, but the redshift and loss of intensity compared to the clean spectrum clearly indicate the presence of carbon. It has been proposed that ethylidyne requires 3-fold symmetric sites to form and that smaller particles present less of these sites, thereby suppressing ethylidyne formation [40,29]. Experimental identification of the carbon species chemical nature after reaction at 300 K was not possible, due to the very low concentration of catalyst used. One possibility is the formation of ethylidene, which was shown to be the likely precursor of ethylidyne on Pt(1 1 1) [41]. If this species is produced at 300 K as a precursor to ethylidyne, then it would in effect have a similar site blocking effect as ethylidyne, as both species would have similar coverages. Ethylidene would have, however, a different chemical interaction with Pt, as it would only be coordinated with two Pt atoms, therefore attenuating its effect on ethylene hydrogenation. Ethylidyne would then be the next species formed at temperatures up to 400 K, and its coordination with three Pt atoms leads to a distinct deactivation of the catalyst, but its relative coverage is the same as ethylidene and therefore CO adsorption properties remain the same.

The measured intensity decrease on the Pt nanoparticles has also been shown on Pt(1 1 1), where the linear CO stretch intensity decreased by a factor of seven when the surface was pretreated with ethylene at 330 K, which led to a saturated coverage of the dehydrogenated product, ethylidyne (upon which ethylene hydrogenation activity is still present) [10,30]. Our results show a factor of 15, but we have only dosed 10 L of CO, whereas the experiment on Pt(1 1 1) was performed in a background CO pressure of 10^{-7} Torr. Additionally, our result showing CO adsorption after the 400 K step is consistent with findings that ethylidyne further dehydrogenates on Pt(1 1 1) only at temperatures above 400 K, which would then lead to a more complete sight blocking [42,43].

Ni presents unexpected behavior as the supported nanoparticles appear to have lost all activity after a few pulses at 300 K as well as all bridge bonded CO (Fig. 3a), but still display a linear CO feature of similar intensity to that of the clean sample (Fig. 3b). It is plausible that the dehydrogenation product at 300 K on Ni is displaced by CO, in contrast to Pt where a signal of small intensity was observed. This behavior has been observed previously on a Ni catalyst supported by silica, where at room temperature the largest IR absorption peak attributed to ethylene disappeared upon CO adsorption [44]. Another possibility is the selective ethylene dehydrogenation on active Ni sites for hydrogenation, in contrast to Pd or Pt where dehydrogenation occurs primarily elsewhere. This also follows our interpretation from the d-band model. Taking into consideration a single active site for hydrogenation on Ni, Pd and Pt, then from our interpretation, ethylene dehydrogenates on Ni exactly at this site with a high probability due to a low activation barrier. On Pt and Pd, the probability to dehydrogenate at an equivalent site is much lower due to a higher activation barrier. In both cases, the activation barrier is a direct result of the d-band center, ε_c^M. This interpretation, however, only requires ethylene dehydrogenation on the active sites on each particle, leaving open the possibility that ethylene dehydrogenation does not occur (as observed on Ni), or does occur (as observed on Pt), on other sites where CO can adsorb. This leads, in the case of Ni, to a very similar CO IR spectrum compared to the clean sample, but the presence of carbon is still observable (loss of bridge bonded and redshifted shoulder in Fig. 3b). For Pt however, the before and after spectra show strong deviations as ethylene dehydrogenates not on an active site (as with Ni) but rather where it competes with CO for adsorption sites. Supporting this point are data from single crystal studies, where the dehydrogenation pathway on Ni proceeds through a vinyl species to acetylene [45], in contrast to Pt where ethylene is known to form ethylidyne from possibly an ethylidene intermediate [41]. These two different reaction pathways indicate a fundamental difference in ethylene dehydrogenation chemistry, which can also be occurring on nanoparticles. Another important aspect to consider is that even though dehydrogenation fragments such as vinyl and ethylidyne form very strong bonds to the surface, their coverages remain relatively low due to repulsive interactions [39]. The large signal intensity of CO on Ni, could also be due to strong repulsive interactions between carbon fragments leaving a large amount of free CO adsorption sites. This puzzling result from Ni indicates that there is still much unknown about the molecular nature of dehydrogenation intermediates and products on small nanoparticles.

5. Conclusion

In conclusion, from pulsed molecular beam experiments of the hydrogenation reaction of ethylene catalyzed by Ni, Pd, and Pt nanoparticles, of 1–1.5 nm size-distribution, we found that the reaction efficiency (TOF) scales with the metal's calculated d-band center, using a 30 atom particle as a model system for the calculations. In this size range of nanoparticles the behavior observed was shown to be that which would be expected from extrapolating bulk properties to this size range, i.e. the calculated d-band center and predicted reactivity of bulk structures are, in this case, scalable down to 1–1.5 nm particles. Specifically, the proclivity for nanoparticle deactivation was observed to decrease in the order Ni > Pd > Pt, following the reverse trend exhibited by the calculated d-band centroid of the clusters, that is $\varepsilon_c^{Ni} < \varepsilon_c^{Pd} < \varepsilon_c^{Pt}$. Clearly, understanding of the molecular details and elucidation of the mechanisms of the involved reactions, require microscopic treatment, beyond the d-electron model used here. Certain aspects that remain unresolved are evidenced by the IRRAS results recorded after running the reaction at 300 K, where a complete deactivation of Ni did not preclude the adsorption of CO. This is indicative of a different interaction and composition of the inhibiting species compared to e.g. Pd, where a complete deactivation was coupled with no CO adsorption. Additionally, Pt showed a very limited CO adsorption after reaction at 300 K even though the activity was measured to be higher per cluster than Pd.

The application of a cluster source for the production of nanoparticles is a powerful tool for explorations of heterogeneous catalytic reaction. Comparative experimental investigations with

respect to the identity of the metal catalysts, in combination with DFT calculations of model systems, can offer insight into subtle differences between the surface chemical behavior within the scalable size range. These basic studies can serve as a foundation for the investigation of size-selected clusters in the sub-nanometer size range (i.e. particles containing up to 20 atoms) where the scalability of these properties breaks down [46,47].

Acknowledgments

B.Y. was supported by the Air Force Office for Scientific Research (AFOSR) and U.L. by Grant No. FG05-86ER45234 from the Office of Basic Energy Sciences of the US Department of energy (DOE). Computations were made at the Gatech Center for Computational Materials Science. The experimental work was supported by an ERC Advanced Grant and the DFG (Project HE 3454/23-1).

References

[1] B. Hammer, J.K. Nørskov, Electronic factors determining the reactivity of metals, Surf. Sci. 343 (1995) 211–220.
[2] B. Hammer, J.K. Nørskov, Theoretical surface science and catalysis, Adv. Catal. 45 (2000) 71.
[3] I. Chorkendorff, J.W. Niemantsverdriet, Concepts of Modern Catalysis and Kinetics, second ed., Wiley-VCH, Weinheim, 2007.
[4] F. Zaera, Hydrogenation and H-D exchange of chemisorbed ethylene on Ni (100) under vacuum, J. Catal. 121 (2) (1990) 318–326, http://dx.doi.org/10.1016/0021-9517(90)90240-K.
[5] C. Egawa, S. Oki, M. Kaneko, N. Minami, I. Suzuki, Ethylene hydrogenation on a Ni(100) surface, Surf. Sci. 427–428 (1999) 268–271, http://dx.doi.org/10.1016/S0039-6028(99)00277-0.
[6] D. Stacchiola, S. Azad, L. Burkholder, W.T. Tysoe, An investigation of the reaction pathway for ethylene hydrogenation on Pd(111), J. Phys. Chem. B 105 (45) (2001) 11233–11239, http://dx.doi.org/10.1021/jp012553h.
[7] H. Molero, D. Stacchiola, W.T. Tysoe, The kinetics of ethylene hydrogenation catalyzed by metallic palladium, Catal. Lett. 101 (3–4) (2005) 145–149, http://dx.doi.org/10.1007/s10562-005-4881-7.
[8] F. Zaera, G.A. Somorjai, Hydrogenation of ethylene over platinum (111) single-crystal surfaces, J. Am. Chem. Soc. 106 (8) (1984) 2288, http://dx.doi.org/10.1021/ja00320a013.
[9] F. Zaera, On the mechanism for the hydrogenation of olefins on transition-metal surfaces: the chemistry of ethylene on Pt(111), Langmuir 12 (1) (1996) 88, http://dx.doi.org/10.1021/la9407020.
[10] P.S. Cremer, X. Su, Y.R. Shen, G.A. Somorjai, Ethylene hydrogenation on Pt(111) monitored in situ at high pressures using sum frequency generation, J. Am. Chem. Soc. 118 (12) (1996) 2942, http://dx.doi.org/10.1021/ja952800t.
[11] A. Tilekaratne, J.P. Simonovis, M.F. López Fagúndez, M. Ebrahimi, F. Zaera, Operando studies of the catalytic hydrogenation of ethylene on Pt(111) single crystal surfaces, ACS Catal. 2 (11) (2012) 2259–2268, http://dx.doi.org/10.1021/cs300411p.
[12] Y. Hadj Romdhane, B. Bellamy, V. De Gouveia, A. Masson, M. Che, Structure sensitivity: hydrogenolysis of n-butane and hydrogenation of ethylene on nickel clusters condensed onto amorphous silica, Appl. Surf. Sci. 31 (3) (1988) 383–401, http://dx.doi.org/10.1016/0169-4332(88)90101-8.
[13] S. Shaikhutdinov, M. Heemeier, M. Bäumer, T. Lear, D. Lennon, R. Oldman, S. Jackson, H.-J. Freund, Structure–reactivity relationships on supported metal model catalysts: adsorption and reaction of ethene and hydrogen on Pd/Al_2O_3/NiAl(110), J. Catal. 200 (2) (2001) 330–339, http://dx.doi.org/10.1006/jcat.2001.3212.
[14] A. Binder, M. Seipenbusch, M. Muhler, G. Kasper, Kinetics and particle size effects in ethene hydrogenation over supported palladium catalysts at atmospheric pressure, J. Catal. 268 (1) (2009) 150–155, http://dx.doi.org/10.1016/j.jcat.2009.09.013.
[15] R.D. Cortright, S.A. Goddard, J.E. Rekoske, J.A. Dumesic, Kinetic study of ethylene hydrogenation, J. Catal. 127 (1) (1991) 342–353, http://dx.doi.org/10.1016/0021-9517(91)90230-2.
[16] R.M. Rioux, H. Song, J.D. Hoefelmeyer, P. Yang, G.A. Somorjai, High-surface-area catalyst design: synthesis, characterization, and reaction studies of platinum nanoparticles in mesoporous SBA-15 silica, J. Phys. Chem. B 109 (6) (2005) 2192, http://dx.doi.org/10.1021/jp048867x.
[17] H. Song, R.M. Rioux, J.D. Hoefelmeyer, R. Komor, K. Niesz, M. Grass, P. Yang, G. A. Somorjai, Hydrothermal growth of mesoporous SBA-15 silica in the presence of PVP-stabilized pt nanoparticles: synthesis, characterization, and catalytic properties, J. Am. Chem. Soc. 128 (9) (2006) 3027–3037, http://dx.doi.org/10.1021/ja057383r.
[18] J. Horiuti, K. Miyahara, Hydrogenation of Ethylene on Metallic Catalysts, NSRDS-NBS (13), 1968.
[19] V. Pallassana, M. Neurock, Electronic factors governing ethylene hydrogenation and dehydrogenation activity of pseudomorphic PdML/Re (0001), PdML/Ru(0001), Pd(111), and PdML/Au(111) surfaces, J. Catal. 191 (2) (2000) 301–317, http://dx.doi.org/10.1006/jcat.1999.2724.
[20] U. Heiz, F. Vanolli, L. Trento, W.-D. Schneider, Chemical reactivity of size-selected supported clusters: an experimental setup, Rev. Sci. Inst. 68 (1997) 1986–1994.
[21] F.F. Schweinberger, A.S. Crampton, T. Zimmermann, G. Kwon, C.J. Ridge, S. Günther, U. Heiz, Submonolayer sensitive adsorption study of trichloroethene on single crystal surfaces by means of MIES, UPS and TPD, Surf. Sci. 609 (2013) 18–29, http://dx.doi.org/10.1016/j.susc.2012.09.005.
[22] S. Kunz, K. Hartl, M. Nesselberger, F.F. Schweinberger, G. Kwon, M. Hanzlik, K.J. J. Mayrhofer, U. Heiz, M. Arenz, Size-selected clusters as heterogeneous model catalysts under applied reaction conditions, Phys. Chem. Chem. Phys. 12 (35) (2010) 10288–10291, http://dx.doi.org/10.1039/C0CP00288G.
[23] M.J. Berr, F.F. Schweinberger, M. Döblinger, K.E. Sanwald, C. Wolff, J. Breimeier, A.S. Crampton, C.J. Ridge, M. Tschurl, U. Heiz, F. Jäckel, J. Feldmann, Size-selected subnanometer cluster catalysts on semiconductor nanocrystal films for atomic scale insight into photocatalysis, Nano Letters 12 (11) (2012) 5903–5906, http://dx.doi.org/10.1021/nl3033069.
[24] K. Wettergren, F.F. Schweinberger, D. Deiana, C.J. Ridge, A.S. Crampton, M.D. Rötzer, T.W. Hansen, V.P. Zhdanov, U. Heiz, C. Langhammer, High sintering resistance of size-selected platinum cluster catalysts by suppressed ostwald ripening, Nano Letters 14 (10) (2014) 5803–5809, http://dx.doi.org/10.1021/nl502686u.
[25] F.F. Schweinberger, Catalysis with Supported Size-selected Pt Clusters, Springer Theses, Springer International Publishing, Switzerland, Cham, 2014.
[26] C. Harding, S. Kunz, V. Habibpour, V. Teslenko, M. Arenz, U. Heiz, Dual pulsed-beam controlled mole fraction studies of the catalytic oxidation of CO on supported pd nanocatalysts, J. Catal. 255 (2) (2008) 234–240, http://dx.doi.org/10.1016/j.jcat.2008.02.008.
[27] Y. Amenomiya, R.F. Pottie, Mass spectra of some deuterated ethanes. I. The effect of ionizing voltage, Can. J. Chem. 46 (10) (1968) 1735–1739, http://dx.doi.org/10.1139/v68-288.
[28] W.G. Durrer, H. Poppa, J.T. Dickinson, C. Park, Decomposition of ethylene on small Pd particles, J. Vac. Sci. Technol. A 3 (3) (1985) 1545–1548, http://dx.doi.org/10.1116/1.573159.
[29] T.P. Beebe Jr., J.T. Yates Jr., Spectroscopic detection of (111) facets on supported pd crystallites: site blocking by ethylidyne on Pd/Al_2O_3, Surf. Sci. 173 (2–3) (1986) L606–L612, http://dx.doi.org/10.1016/0039-6028(86)90186-X.
[30] P. Chen, K.Y. Kung, Y.R. Shen, G.A. Somorjai, Sum frequency generation spectroscopic study of CO/ethylene coadsorption on the Pt(111) surface and CO poisoning of catalytic ethylene hydrogenation, Surf. Sci. 494 (3) (2001) 289–297, http://dx.doi.org/10.1016/S0039-6028(01)01512-6.
[31] R.M. Rioux, J.D. Hoefelmeyer, M. Grass, H. Song, K. Niesz, P. Yang, G.A. Somorjai, Adsorption and co-adsorption of ethylene and carbon monoxide on silica-supported monodisperse pt nanoparticles: volumetric adsorption and infrared spectroscopy studies, Langmuir 24 (1) (2008) 198–207, http://dx.doi.org/10.1021/la702685a.
[32] M.J. Lundwall, S.M. McClure, D.W. Goodman, Probing terrace and step sites on pt nanoparticles using CO and ethylene, J. Phys. Chem. C 114 (17) (2010) 7904, http://dx.doi.org/10.1021/jp9119292.
[33] B. Yoon, U. Landman, V. Habibpour, C. Harding, S. Kunz, U. Heiz, M. Moseler, M. Walter, Oxidation of magnesia-supported Pd30 nanoclusters and catalyzed CO combustion: size-selected experiments and first-principles theory, J. Phys. Chem. C 116 (17) (2012) 9594–9607, http://dx.doi.org/10.1021/jp301314s.
[34] G. Kresse, D. Joubert, From ultrasoft pseudopotentials to the projector augmented-wave method, Phys. Rev. B 59 (3) (1999) 1758–1775, http://dx.doi.org/10.1103/PhysRevB.59.1758.
[35] J.P. Perdew, K. Burke, M. Ernzerhof, Generalized gradient approximation made simple, Phys. Rev. Lett. 77 (18) (1996) 3865–3868, http://dx.doi.org/10.1103/PhysRevLett.77.3865.
[36] M. Moseler, H. Häkkinen, R.N. Barnett, U. Landman, Structure and magnetism of neutral and anionic palladium clusters, Phys. Rev. Lett. 86 (12) (2001) 2545–2548, http://dx.doi.org/10.1103/PhysRevLett.86.2545.
[37] M. Moseler, H. Häkkinen, U. Landman, Supported magnetic nanoclusters: soft landing of Pd clusters on a MgO surface, Phys. Rev. Lett. 89 (17) (2002) 176103, http://dx.doi.org/10.1103/PhysRevLett.89.176103.
[38] A. Ruban, B. Hammer, P. Stoltze, H.L. Skriver, J.K. Nørskov, Surface electronic structure and reactivity of transition and noble metals, J. Mol. Catal. A 115 (3) (1997) 421–429, http://dx.doi.org/10.1016/S1381-1169(96)00348-2.
[39] U. Starke, A. Barbieri, N. Materer, M.A. Van Hove, G.A. Somorjai, Ethylidyne on Pt(111): determination of adsorption site, substrate relaxation and coverage by automated tensor LEED, Surf. Sci. 286 (1–2) (1993) 1–14, http://dx.doi.org/10.1016/0039-6028(93)90551-T.
[40] T.P. Beebe, J.T. Yates, An in situ infrared spectroscopic investigation of the role of ethylidyne in the ethylene hydrogenation reaction on palladium/alumina, J. Am. Chem. Soc. 108 (4) (1986) 663–671, http://dx.doi.org/10.1021/ja00264a016.
[41] F. Zaera, T.V. Janssens, H. Öfner, Reflection absorption infrared spectroscopy and kinetic studies of the reactivity of ethylene on Pt(111) surfaces, Surf. Sci. 368 (1–3) (1996) 371, http://dx.doi.org/10.1016/S0039-6028 96 01078-3.
[42] J. Creighton, J. White, A SIMS study of the dehydrogenation of ethylene on Pt (111), Surf. Sci. 129 (2–3) (1983) 327, http://dx.doi.org/10.1016/0039-6028(83)90183-8.
[43] T.A. Land, T. Michely, R.J. Behm, J.C. Hemminger, G. Comsa, Direct observation of surface reactions by scanning tunneling microscopy:

ethylene>ethylidyne>carbon particles>graphite on Pt(111), J. Chem. Phys. 97 (9) (1992) 6774–6783, http://dx.doi.org/10.1063/1.463655.
[44] M. Primet, N. Sheppard, Modifications of the infrared spectra from chemisorbed CO as a measure of hydrogen coverage of a nickel surface: dependence of the spectra of chemisorbed ethylene on hydrogen coverage, J. Catal. 41 (2) (1976) 258–270, http://dx.doi.org/10.1016/0021-9517(76)90341-9.
[45] F. Zaera, R.B. Hall, High-resolution electron energy loss spectroscopy and thermal programmed desorption studies of the chemisorption and thermal decomposition of ethylene and acetylene on nickel(100) single-crystal surfaces, J. Phys. Chem. 91 (16) (1987) 4318–4323, http://dx.doi.org/10.1021/j100300a023.
[46] U. Heiz, U. Landman, P. Avouris, B. Bhushan, D. Bimberg, K. von Klitzing, H. Sakaki, R. Wiesendanger (Eds.), Nanocatalysis, Nanoscience and Technology, Springer Berlin Heidelberg, Berlin, Heidelberg, 2007.
[47] U. Landman, B. Yoon, C. Zhang, U. Heiz, M. Arenz, Factors in gold nanocatalysis: oxidation of CO in the non-scalable size regime, Top. Catal. 44 (1–2) (2007) 145–158, http://dx.doi.org/10.1007/s11244-007-0288-6.